International Journal of Multiphase Flow 99 (2018) 423–436

Contents lists available at ScienceDirect

International Journal of Multiphase Flow

journal homepage: www.elsevier.com/locate/ijmulflow

Air-water flow properties in stepped chutes with modified step and cavity geometries

Gangfu Zhang*, Hubert Chanson

School of Civil Engineering, University of Queensland, Brisbane QLD 4072, Australia

ARTICLE INFO

Article history:
Received 30 June 2017
Revised 3 November 2017
Accepted 10 November 2017
Available online 15 November 2017

Keywords:
Multiphase flow
Air entrainment
Turbulence
Stepped spillway
Macro-roughness
Chamfer
Physical modelling

ABSTRACT

Skimming air-water flow properties were investigated in a stepped chute configured with triangular steps, chamfered steps, and partially blocked step cavities. The turbulent interactions between air and water were examined using a synchronised system consisting of a dual-tip phase-detection probe and a pressure transducer mounted side-by-side. In comparison to uniform triangular steps, the chamfered steps were found to cause a reduction in air entrainment and an increase in mean velocity gradient next to the pseudo-bottom. Partial cavity blockages appeared to have little effect on air entrainment, but were linked to an increased presence of large-scale structures in the overflow, which likely resulted from a reduction in mutual sheltering between adjacent step elements. The results indicated that modifications of step and cavity geometries might have significant implications on stepped chute design.

1. Introduction

Naturally occurring gas-liquid flows are one of the most challenging hydraulic problems in consequence of the involvement of deformable interfaces and gas compressibility. One classic example is the self-aerated skimming flow in a stepped chute, occurring due to interactions between turbulent boundary layer and free-surface (e.g. Rao and Kobus 1971, Wood 1991, Chanson 1997). The air-water mixture downstream of the inception point of aeration is characterised by highly complicated three-dimensional turbulent processes. An example of prototype stepped chute skimming flow is illustrated in Fig. 1.

The properties and structures of aerated skimming flows were examined by many past studies (e.g. Chanson 1997, Chanson and Toombes 2002, Felder and Chanson 2014a, 2016). To date, most experimental observations are limited to flat steps within prismatic rectangular channels. Several experiments performed for modified bottom geometries have demonstrated modifications of energy dissipation and aeration performance to different extents (e.g. Stephenson (1988) on varying step sizes, Gonzalez and Chanson (2008) on steps with vanes, Felder and Chanson (2014b) on pooled steps, Wuthrich and Chanson (2015) and Zhang and Chanson (2016a) on gabion steps). It is of interest to investigate how modified bottom geometries would affect the air-water flow properties in a stepped chute.

The goal of the present study is to investigate the effects of modified step edge and cavity shapes on the two-phase flow properties in aerated skimming flows over stepped chutes. Detailed air-water measurements were performed in stepped chutes configured with triangular steps, chamfered steps, and partially blocked step cavities. The complex two-phase interactions were characterised using a synchronised setup consisting of a dual-tip phase-detection probe mounted abreast of a total pressure transducer. The results revealed some effects of step edge and cavity geometries on air-entrainment and flow structures, which underlined the complexity of stepped chute flows.

2. Experimental facilities and instrumentation

2.1. Inflow conditions

Present investigations were conducted in a large-size stepped spillway model at the University of Queensland (UQ) with very-calm inflow conditions. A smooth and stable discharge was delivered by three pumps driven by adjustable frequency AC motors. Water was fed into a 1.7 m deep, 5 m wide intake basin with a surface area of 2.7×5 m^2, leading to a 2.8 m long side-wall convergent with a contraction ratio of 5.08:1, which resulted in a smooth and waveless inflow. The chute inflow was controlled by an upstream broad crested weir. The weir consists of a 1.2 m high, 0.6 m

* Corresponding author.
E-mail addresses: g.zhang3@uq.edu.au (G. Zhang), h.chanson@uq.edu.au (H. Chanson).

https://doi.org/10.1016/j.ijmultiphaseflow.2017.11.009
0301-9322/

Fig. 1. Hinze dam (Gold Coast, Australia) spillway in operation on 31 Mar 2017 – $q_w \approx 27$ m^2/s, $d_c/h \approx 3.5$, $Re \approx 1.0 \times 10^8$.

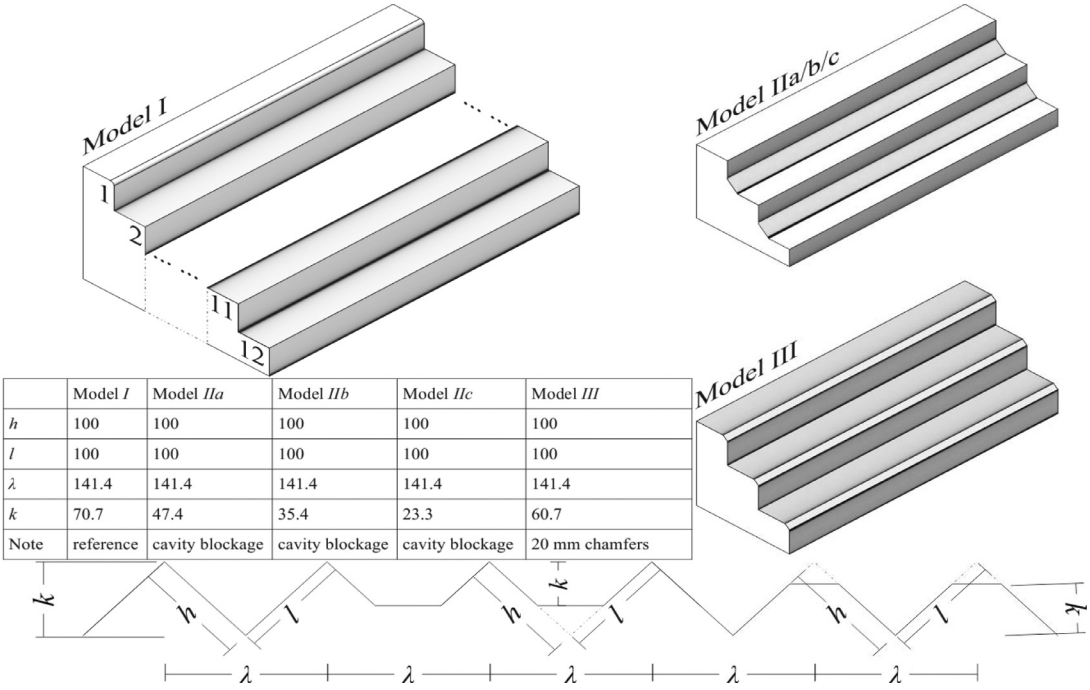

	Model *I*	Model *IIa*	Model *IIb*	Model *IIc*	Model *III*
h	100	100	100	100	100
l	100	100	100	100	100
λ	141.4	141.4	141.4	141.4	141.4
k	70.7	47.4	35.4	23.3	60.7
Note	reference	cavity blockage	cavity blockage	cavity blockage	20 mm chamfers

Fig. 2. Definition sketch of experimental configurations (units: mm).

long and 0.985 m wide crest with a vertical upstream wall, an upstream rounded nose (0.058 m radius), and a downstream rounded edge (0.012 m radius). The crest was made of smooth, painted marine ply. The discharge was deduced from integration of velocity profiles measured on the crest (Zhang and Chanson 2016b).

2.2. Stepped spillway models

Detailed two-phase flow studies were conducted in a 45° stepped chute configured with uniform triangular steps and with several modifications to step shape and cavity geometries. The chute details are sketched in Fig. 2 and summarised in Table 1. Initial experiments were performed with twelve identical triangular steps ($0.1 \times 0.1 \times 1$ m, Fig. 2, top-left). Additional studies were undertaken for three cases of modified cavity geometries, where the step cavities were blocked to 33%, 50%, and 66% of the step height, corresponding to roughness densities $\lambda/k = 3$, 4, 6 (Fig. 2, top-right), with λ the streamwise separation between adjacent step edges and k the step roughness height. Finally, the effects of step edge modification were examined by replacing step edges 2 – 12 with 20 mm chamfers (Fig. 2, bottom-right).

Table 1
Experimental channel details.

Model	*h* (m)	*l* (m)	λ (m)	*k* (m)	λ/*k*	θ (°)	Modification
I	0.1	0.1	0.14	0.071	2	45	Smooth triangular cavities (i.e. no modification)
IIa	0.1	0.1	0.14	0.047	3	45	Partially
IIb				0.035	4		filled
IIc				0.024	6		cavities
III	0.1	0.1	0.14	0.061	2.33	45	Chamfered step edges

Notes: *h* – vertical step height; *l* – step length; λ – roughness wavelength; *k* – roughness height; θ – chute slope.

Table 2
Experimental flow conditions for detailed clear-water and air-water flow measurements.

Model	θ (°)	h (m)	W (m)	λ/k	Location	Q (m^3/s)	d_c/h	Re	Instrumentation*1
I	45	0.1	1.0	2	Step edges 5 – 12	0.057 – 0.216	0.70 – 1.70	$2.3 - 8.8 \times 10^5$	DPP: 20 kHz/45 s
					Step edges 5 – 12	0.083 – 0.216	0.90 – 1.70	$3.4 - 8.8 \times 10^5$	DPP/TPT: 5 kHz/180s
IIa	45	0.1	1.0	3	Step edges 4 – 12	0.083 – 0.216	0.90 – 1.70	$3.4 - 8.8 \times 10^5$	DPP: 20 kHz/45 s
					Step edges 3 – 12	0.083 – 0.182	0.94 – 1.75	$3.6 - 9.1 \times 10^5$	DPP/TPT: 5 kHz/180 s
IIb	45	0.1	1.0	4	Step edges 4 – 12	0.083 – 0.216	0.90 – 1.70	$3.4 - 8.8 \times 10^5$	DPP: 20 kHz/45 s
IIc	45	0.1	1.0	6	Step edges 4 – 12	0.083 – 0.216	0.90 – 1.70	$3.4 - 8.8 \times 10^5$	DPP: 20 kHz/45 s
III	45	0.1	1.0	2.33	Step edges 5 – 12	0.083 – 0.182	0.90 – 1.50	$3.4 - 7.3 \times 10^5$	DPP: 20 kHz/45 s DPP/TPT: 5 kHz/180 s

Notes: *1 – DPP: Dual-tip Phase-detection probe; TPT: Total pressure transducer.

2.3. Instrumentation and experimental flow conditions

The present experiments were performed with water discharges ranging between $Q = 0.083$ and 0.216 m^3/s, with a focus on the skimming flow regime. The corresponding Reynolds number range was $3.4 - 8.8 \times 10^5$. For all models, the air-water flow properties were recorded with dual-tip phase-detection probes with an inner tip diameter of 0.25 mm and longitudinal tip separations Δx between 4.3 and 8 mm. For models *I* and *IIa*, additional data were obtained by simultaneously sampling a dual-tip phase-detection probe mounted abreast of a total pressure transducer (inner diameter: 1 mm; outer diameter: 4 mm) to further characterise the turbulent air-water interactions. The pressure transducer was calibrated to measure relative pressures between 0 and 0.15 bars at a precision of 0.5% full scale (FS). The details of the experimental flow conditions and sampling parameters are summarised in Table 2.

3. Air-water flow properties

3.1. Basic air-water flow properties

Basic air-water properties at step edges were investigated for all step roughness types for skimming flow discharges ranging between $d_c/h = 0.9$ – 1.5, where d_c is the critical flow depth, and h the step height. For all models, the aerated flow was divided into an initial rapidly varied flow (RVF) region immediately downstream of the inception point of free-surface aeration, followed by a gradually varied flow region (GVF). In the RVF region, advective transport is negligible compared with turbulent diffusion, and the void fraction profiles may be modelled with a theoretical solution (Zhang and Chanson 2017):

$$C = \frac{1}{2}\text{erfc}\left(\frac{Y_{50} - y}{2\sqrt{D_a t}}\right) \quad (1)$$

where C is the void fraction, y is the normal distance measured from the pseudo-bottom, Y_{50} the elevation where $C = 0.5$, t is the diffusion time, and D_a is an average diffusivity:

$$D_a = \frac{1}{t}\int_0^t D_t dt \quad (2)$$

where D_t is a turbulent diffusivity. The similarity between Eq. (1) and a Gaussian cumulative distribution function (CDF) with a mean of Y_{50} and standard deviation of $\sqrt{2D_a t}$ emphasises the random nature of the initial diffusion process.

Further downstream, the aerated flow approaches an approximate equilibrium, where the effects of bubble buoyancy and droplet weight become relevant. Assuming a homogeneous air-water mixture between $C = 0$ and 0.9 (Wood 1985; Chanson 1993), a solution is obtained by balancing the turbulent diffusion and advection terms in the advection-diffusion equation (Chanson and Toombes 2002):

$$C = 1 - \tanh^2\left[K - \frac{y'}{2D_0} + \frac{\left(y' - \frac{1}{3}\right)^3}{3D_0}\right] \quad (3)$$

where Y_{90} is the elevation where $C = 0.9$, K is an integration constant and D_0 is a function of C_{mean}:

$$C_{mean} = \frac{1}{Y_{90}}\int_0^{Y_{90}} C dy \quad (4)$$

$$K = \tanh^{-1}\left(\sqrt{0.1}\right) + \frac{1}{2D_0} - \frac{8}{81D_0} \quad (5)$$

$$D_0 = -\frac{1}{3.614}\ln\left(1.0434 - \frac{C_{mean}}{0.7622}\right) \quad (6)$$

Fig. 3 presents the dimensionless step edge void fraction distributions in all setups for a skimming flow $d_c/h = 0.9$, where x is the streamwise distance measured from the first step edge, x_i is the inception point location, and λ is the separation between adjacent step edges (= 0.141 m). The theoretical solutions (Eqs. (1) and (3)) were also plotted for ease of reference. A good agreement between experimental data and theoretical models was observed for all models with sharp edges (i.e. models *I, IIa, IIb, IIc*). In model *III* (Figs. 3e and f), the no-flux boundary condition at the chamfer surface appeared to be associated with the build-up of some air-concentration boundary layer. The observation was consistent with those in chute and tunnel spillways, and might contribute to a reduction in skin friction (Chanson 2004). The results suggested that the air concentration profiles were more influenced by step edge profiles than by cavity shapes.

The bubble count rate F is defined as half the number of air-water interfaces detected by the probe sensor per second. For a given interfacial velocity, it is directly proportional to the specific interfacial area (Chanson 2001). Fig. 4 presents typical skimming flow bubble count rate distributions in all setups for a dimensionless discharge $d_c/h = 0.9$. All data exhibited a characteristic bell shape with a marked maximum at $y/Y_{50} \approx 1$ ($C \approx 0.5$), consistent with previous studies (e.g. Chanson and Toombes 2002; Toombes and Chanson 2008). Furthermore, a continuous increase in maximum bubble count rate with increasing distance downstream of the inception was observed in all setups, implying that uniform equilibrium conditions were not achieved. Overall, the step edge and cavity modifications appear to have no significant influence on the bubble count rate profiles.

The interfacial velocity may be derived from the cross-correlation function between two probe signals (Crowe et al., 1998; Chanson 2002; Chanson and Carosi 2007):

$$U_{aw} = \frac{\Delta x}{T_{aw}} \quad (7)$$

where U_{aw} is the interfacial velocity, Δx is the streamwise tip separation and T_{aw} is the time lag at which the cross-correlation function peaks. Fig. 5 shows the step edge interfacial velocity profiles

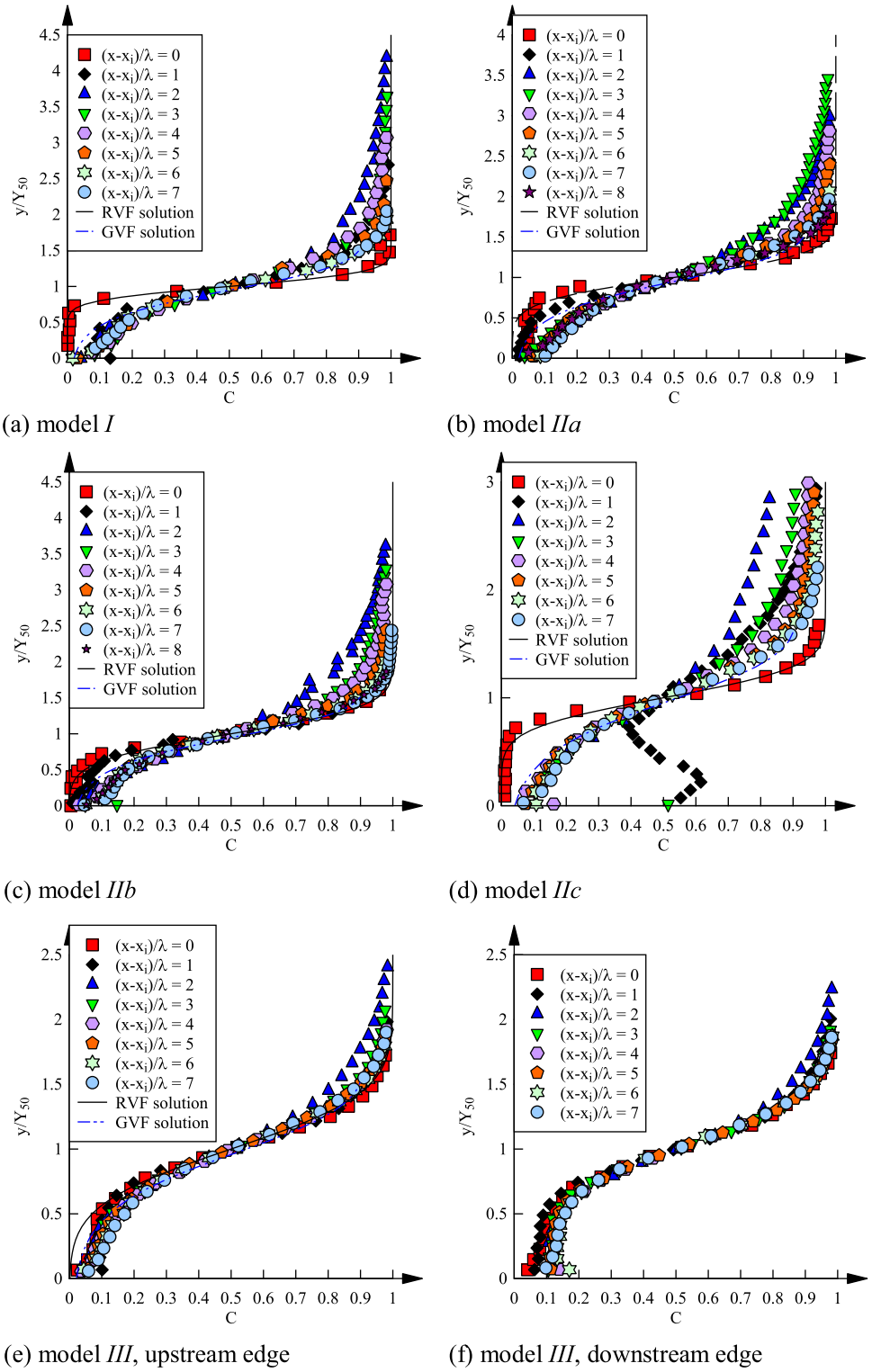

Fig. 3. Step edge void fraction distributions in chutes with various step roughness types. Flow conditions: $d_c/h = 0.9$, $Re = 3.4 \times 10^5$, $\theta = 45°$.

for all models, where U_{50} is the interfacial velocity corresponding to $C = 0.5$. All data followed a two-tier distribution:

$$\frac{U_{aw}}{U_{50}} = \left(\frac{y}{Y_{50}}\right)^{\frac{1}{N_{50}}} \quad \text{for } 0 \le y/Y_{50} < 1 \tag{8}$$

and

$$\frac{U_{aw}}{U_{50}} = 1 \quad \text{for } y/Y_{50} \ge 1 \tag{9}$$

Eqs. (8) and (9) imply a physical demarcation in terms of the flow composition at about y/Y_{50}=1. A constant interfacial velocity profile for $y/Y_{50} > 1$ implied lesser shear stress in this region, despite the visually complex nature of the mixture. It also appeared that the dynamics of air had little observable effect on the mean momentum of the water droplets in the spray zone ($C > 0.9$). Table 3 summarises the best fit of power law exponent N_{50}, and corresponding correlation coefficients R. For all present data, N_{50}

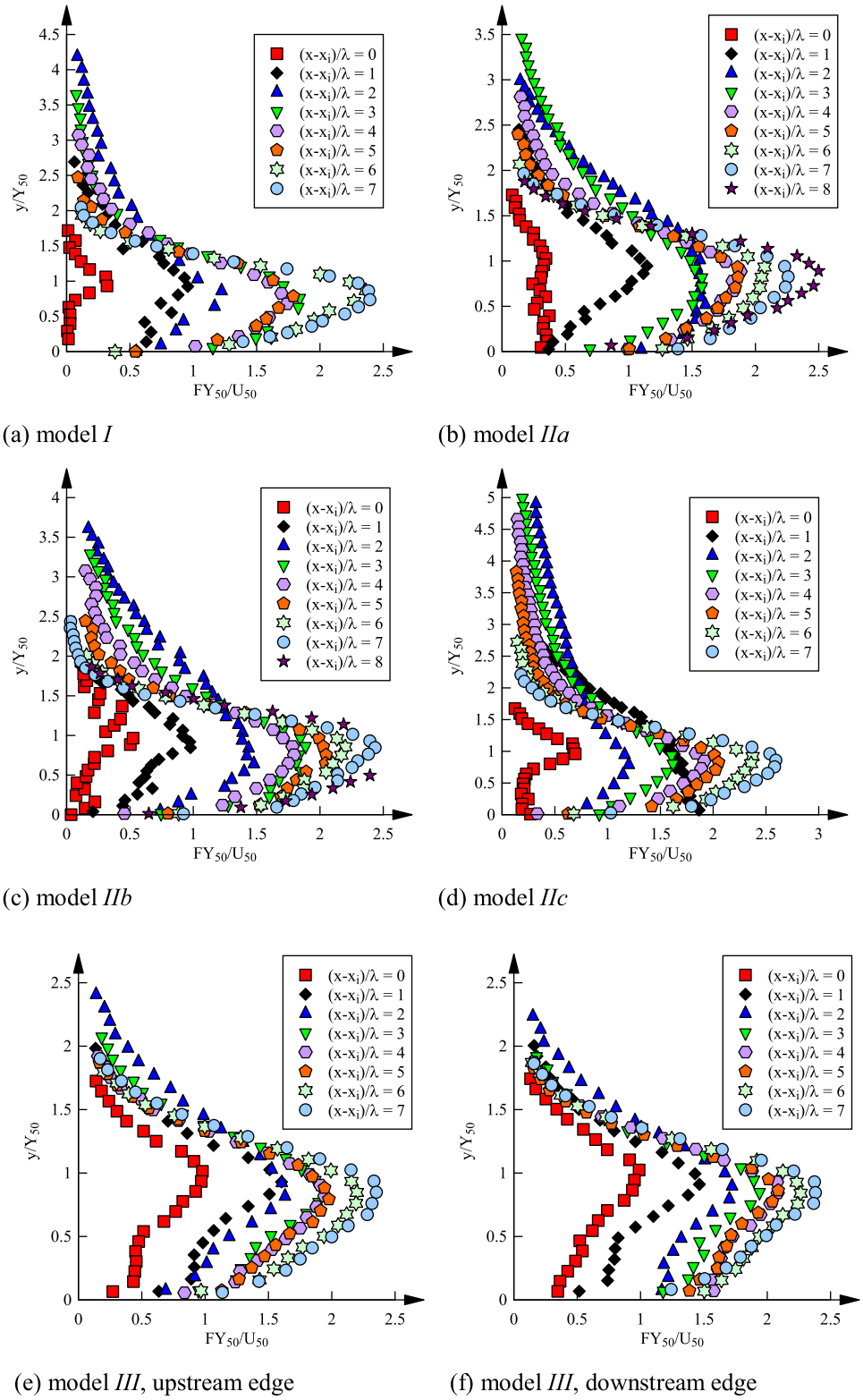

Fig. 4. Step edge bubble count rate distributions in chutes with various step roughness types. Flow conditions: $d_c/h = 0.9$, $Re = 3.4 \times 10^5$, $\theta = 45°$.

ranged between 3.1 – 7.6. Compared to the non-modified chute (*I*), those with modified step cavities (*IIa,b,c*) recorded smaller N_{50} values, possibly linked to a downward shift in the mean velocity profile. In the chamfered chute (*III*), the N_{50} values were larger at the upstream edge than at the downstream chamfer edge, which could be linked to some flow separation at the upstream edge. Furthermore, the cavity and step edge modifications appeared to have respectively resulted in a decrease and an increase in the correlation coefficient *R*. The observation was likely reflective of geometry-induced changes in vortex shedding behaviours, which in turn lead to some streamwise variations in the overflow.

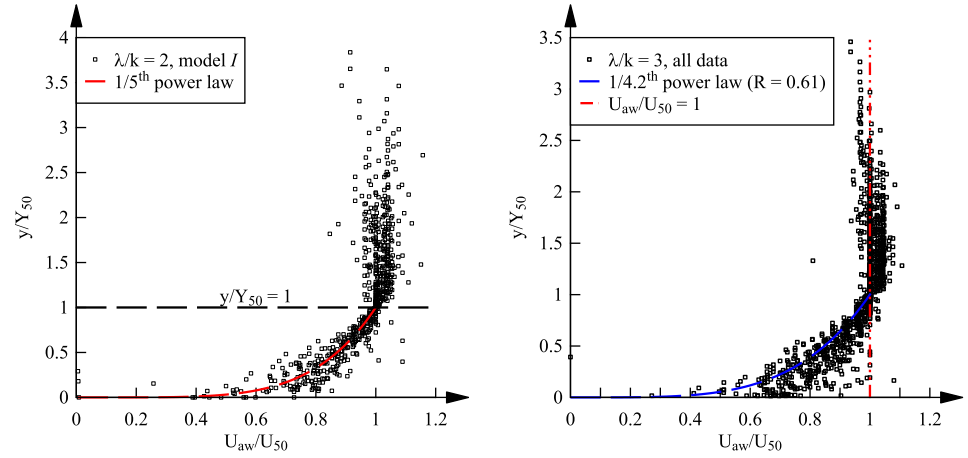

(a) model *I*

(b) model *IIa*

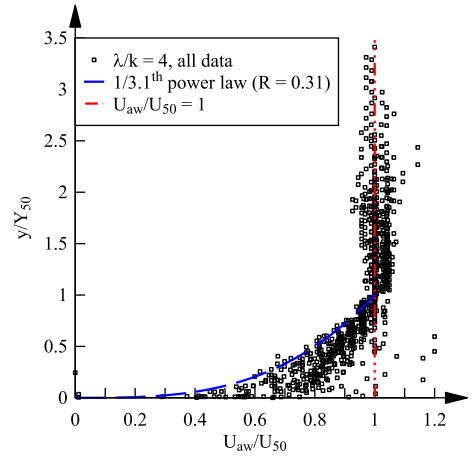

(c) model *IIb*

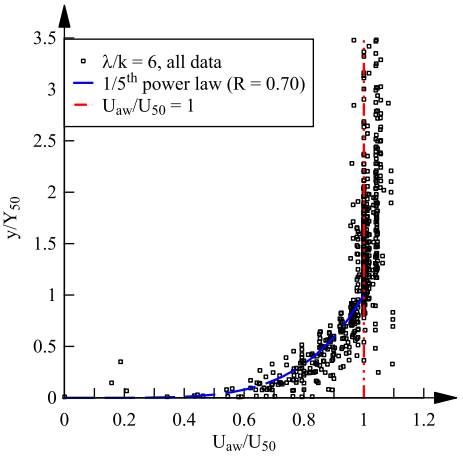

(d) model *IIc*

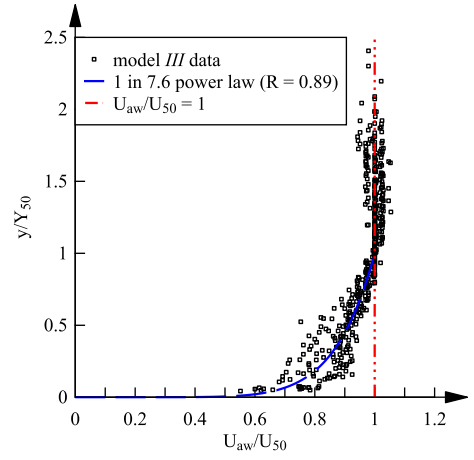

(e) model *III*, upstream edge

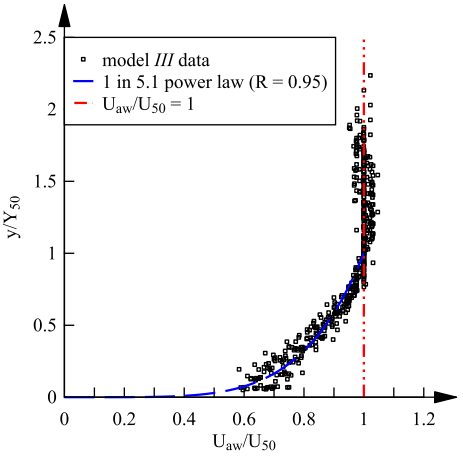

(f) model *III*, downstream edge

Fig. 5. Interfacial velocity distributions at step edges in chutes with various step roughness types. Flow conditions: $d_c/h = 0.9$ – 1.7, $Re = 3.4$ – 8.8×10^5, $\theta = 45°$.

3.2. Interfacial turbulence characteristics

The fluctuations of interfacial velocity may be quantified by comparing the relative widths between auto- and cross-correlation functions of the two tip signals (Chanson and Toombes 2002):

$$Tu_{aw} = 0.85 \frac{\sqrt{\tau_{0.5}^2 - T_{0.5}^2}}{T_{aw}} = \frac{\sqrt{\overline{u'^2_{aw}}}}{U_{aw}} \quad (10)$$

where Tu_{aw} is the interfacial turbulence intensity, $\tau_{0.5}$ is the time lag where the normalised cross-correlation function between two probe sensors equals 0.5, $T_{0.5}$ is the time lag for which the normalised auto-correlation function equals 0.5, T_{aw} is the time lag corresponding to the peak of the cross-correlation function between two tips, and u'_{aw} is the interfacial velocity fluctuation. For a given probe tip separation, a large relative width between auto-

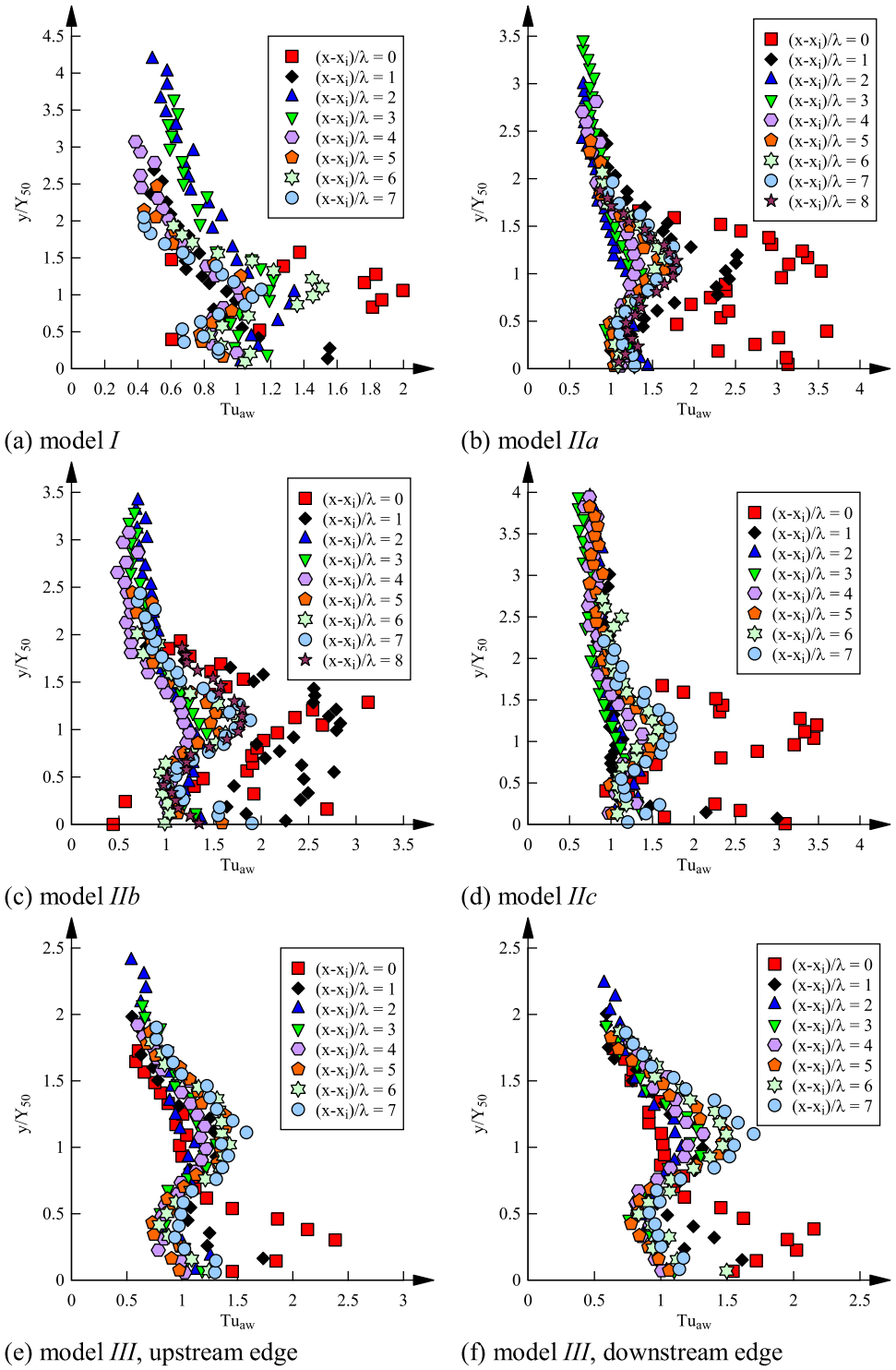

Fig. 6. Interfacial turbulence intensity distributions at step edges in chutes with various step roughness types. Flow conditions: $d_c/h = 0.9$, $Re = 3.4 \times 10^5$, $\theta = 45°$.

and cross-correlation functions must correspond to large fluctuations of the air-water interfaces (Chanson and Carosi 2007). Implicitly, Tu_{aw} takes into account all forms of interfacial fluctuations whether they are turbulence-induced rigid-body transformations (which preserve angles and line lengths) or deformation of the interfaces (warping).

Fig. 6 shows typical interfacial turbulence intensity distributions at step edges for a skimming flow $d_c/h = 0.9$. For all models, the inception point data showed some large scatter that reflected the unsteady nature of the region. Further downstream, the data generally followed a characteristic shape, with local maxima next to the pseudo-bottom and at about $y/Y_{50} = 1$. The observations were consistent with past studies in skimming flows (e.g. Chanson and Carosi 2007, Felder and Chanson 2009). The two peaks in Tu_{aw} were respectively associated with large turbulence levels in the step-induced wakes, and a continuous breakdown of freshly entrained air coupled with a phase change process. For $y/Y_{50} > 1$ the data decreased monotonically with increasing elevation. At suffi-

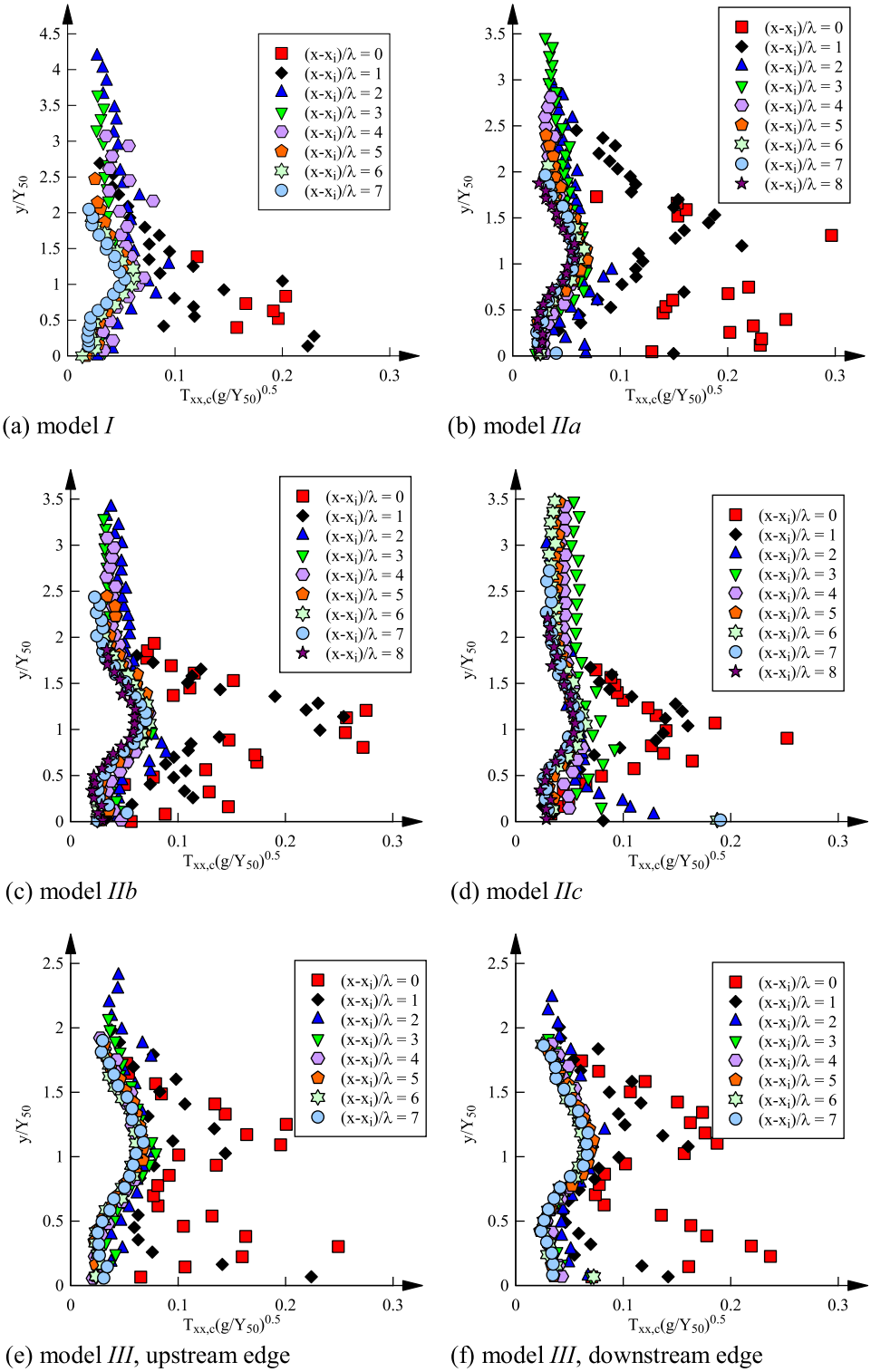

Fig. 7. Integral air-water time scale distributions at step edges in chutes with various step roughness types. Flow conditions: $d_c/h = 0.9$, $Re = 3.4 \times 10^5$, $\theta = 45°$.

ciently high elevations the flow was mainly composed of discrete droplets, and the strain field of the surrounding air had little effect on the water because of the large density difference. The non-trivial Tu_{aw} values (>0.5) in this region most likely resulted from inhomogeneous droplet shapes instead of turbulence. A comparison between the different models revealed the largest Tu_{aw} for the modified cavities, followed by those for the chamfered steps and for the unmodified chute. The observation suggested that interfacial turbulence might be sensitive to additional length scales introduced by modifications of step and cavity shapes.

Following Chanson and Carosi (2007), an integral air-water time scale may be determined from the autocorrelation function of an air-water voltage signal:

$$T_{xx,c} = \int_0^{\tau_{R_{xx,c}=0}} R_{xx,c}(\tau) d\tau \tag{11}$$

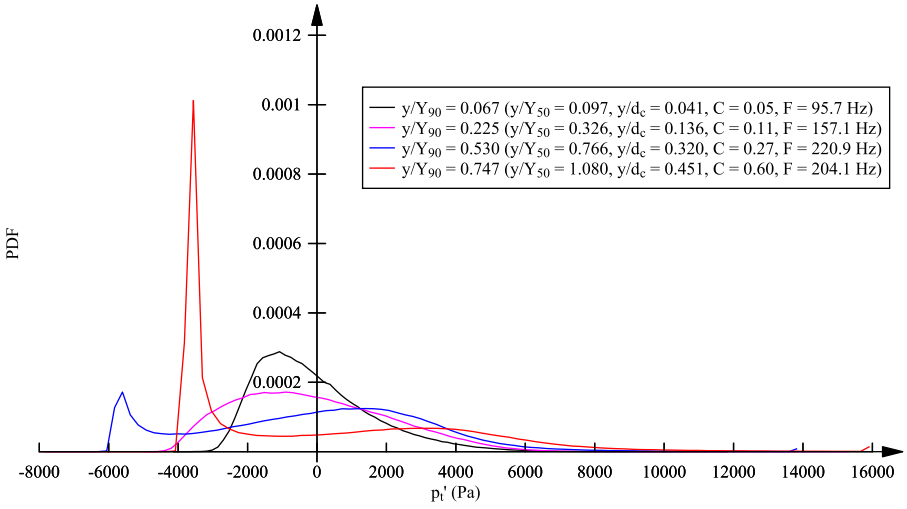

Fig. 8. Typical PDFs of total pressure fluctuations in the air-water flow region in skimming flows – Flow conditions: $d_c/h = 0.9$, $\theta = 45°$, model *I*, step edge 12.

Table 3
Interfacial velocity power law exponents in all present configurations (average over all data).

Model	N_{50}	R	Remark
I	5.0	0.75	λ/k = 2, triangular steps
IIa	4.2	0.61	λ/k = 3, partially blocked cavities
IIb	3.1	0.31	λ/k = 4, partially blocked cavities
IIc	5.0	0.70	λ/k = 6, partially blocked cavities
III (upstream edge)	7.6	0.89	λ/k = 2.33, chamfered steps
III (downstream edge)	5.1	0.95	λ/k = 2.33, chamfered steps

where $R_{xx,c}$ is the normalised autocorrelation coefficient of the void fraction signal and τ is the time lag. $T_{xx,c}$ is a time scale that characterises the longest streamwise air-water connections (i.e. air-water 'memory' time). Fig. 7 presents the $T_{xx,c}$ distributions at step edges for a skimming flow discharge $d_c/h = 0.9$. All data followed a bell shape with a maximum at $y/Y_{50} \approx 1$. In addition, a local maximum was sometimes observed next to the pseudo-bottom, which could be linked to vortices shed from the step edge. Some large data scatter was seen for the first 2 – 3 step edges downstream of the inception point because of boundary layer fluctuations. Further downstream, the data tended to become approximately self-similar, as previously observed (Carosi and Chanson 2006; Felder 2013). The finding suggested that the air-diffusion layer could attain some local equilibrium at sufficient distance downstream of the inception point. The step edge and cavity modifications appeared to bear no significant effect on the air-water time scale distributions.

4. Two-phase interactions

4.1. Total pressure fluctuations

The total pressure fluctuations in the aerated flow region were examined for all models with a total pressure transducer. The sensor responded to both turbulence-induced and density-induced fluctuations, as shown in Fig. 8. Next to the pseudo-bottom, the PDF of the fluctuating total pressure p'_t was typically unimodal with a positive skew, likely associated with intermittent fluid ejections from the step cavity. With increasing distance from the pseudo-bottom the PDF curves became distinctively bimodal because of density fluctuations, while some bias due to wetting and drying were also likely. Importantly, Fig. 8 implies that any second or higher order statistics of total pressure fluctuations would be determined by the combined effects of density and isolated-phase (air or water) fluctuations.

An intensity of total pressure fluctuation may be defined as:

$$\frac{\sqrt{\overline{p_t'^2}}}{P_t} \quad (12)$$

where p'_t and P_t are respectively the fluctuating and mean total pressure measured by the total pressure sensor. Fig. 9 presents typical distributions of total pressure fluctuation intensity at step edges for a skimming flow $d_c/h = 0.9$. For all models, the total pressure fluctuation intensity exhibited a minimum at about $y/Y_{50} = 0.6$, where the void fraction C was about 0.2 – 0.3. The total pressure fluctuations intensified next to the pseudo-bottom and towards the free-surface, respectively on account of a high turbulence level and density fluctuations coupled with a diminishing mean total pressure P_t. Note that the influence due to capillary effects might grow near the free-surface. Overall, the data highlighted the turbulent nature of the skimming stepped chute flow. No significant difference was observed between the unmodified model and those with altered step and cavity geometries.

4.2. Water-phase turbulence

The stepped spillway flow is characterised by extremely complex interactions between the air and water phases. The lowest order descriptor of the water phase turbulence is the turbulence intensity, defined as:

$$Tu_p = \frac{\sqrt{\overline{u_w'^2}}}{U_w} \quad (13)$$

where u'_w and U_w are the fluctuating and mean water velocities. The turbulence intensity Tu_p may be estimated from simultaneously sampled total pressure and phase-detection probe signals (Zhang and Chanson 2016b):

$$Tu_p = \sqrt{\frac{\frac{\overline{p_t'^2}}{\rho_w^2 U_w^4} - \frac{1}{4}C(1-C)}{\left(1+\frac{1}{2}C\right)(1-C)}} \quad (14)$$

where the total pressure fluctuation p'_t and the void fraction C are measured by the pressure transducer and phase-detection probe, respectively. Note that the validity of Eq. (14) decreases for Tu_p greater than 0.4 – 0.5. Tu_p characterises the streamwise velocity fluctuations of water particles and may be biased by: (a) instantaneous pressure rise due to surface tension during interfacial

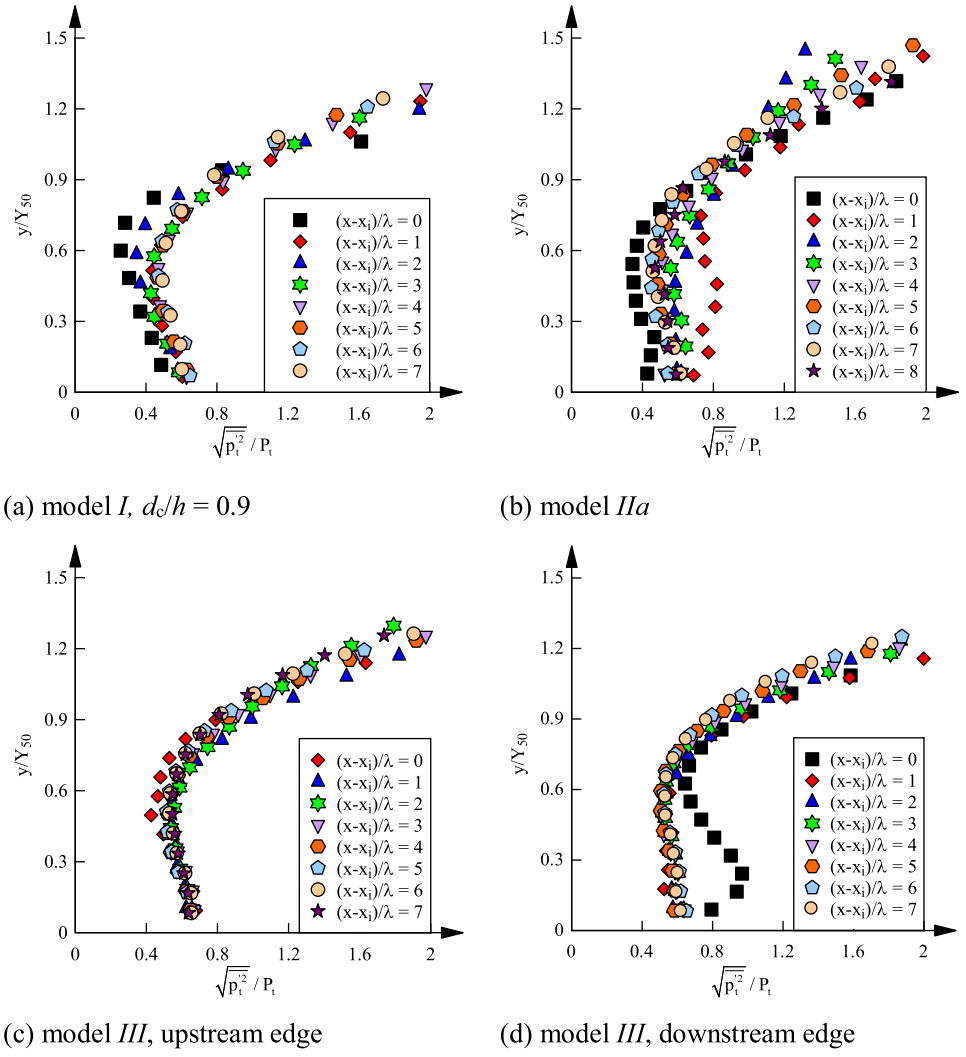

Fig. 9. Total pressure fluctuation intensity distributions at step edges. Flow conditions: model *I*/*III*: $d_c/h = 0.9$, $Re = 3.4 \times 10^5$; model *IIa*: $d_c/h = 0.94$, $Re = 3.6 \times 10^5$; $\theta = 45°$.

processes; (b) wetting and drying time of the sensor diaphragm; (c) bursting bubbles. Lastly, in high void fraction regions the water-phase is no longer continuous, and Eq. (14) essentially reflects the velocity variations over a streamwise ensemble of water droplets.

Typical water phase turbulence intensity distributions at step edges are presented in Fig. 10 for a skimming flow $d_c/h = 0.9$. The data were shown up to $y = Y_{50}$ because of different flow structures in the upper region. Herein the mean water velocity U_w was calculated from the mean total pressure P_t assuming a hydrostatic pressure distribution between $0 \le y \le Y_{90}$. All data typically ranged between 0.1 – 0.5, approximately an order of magnitude smaller than the largest interfacial turbulence intensity Tu_{aw}. Hence bubbles should not be used as accurate tracers of water-phase turbulence. Albeit some scatter, the Tu_p levels was about 30% at the pseudo-bottom, and decreased to 10% – 20% at $y/Y_{50} = 0.7$ – 0.8. These values were comparable to those obtained in the clear-water flow region in a stepped chute (Ohtsu and Yasuda 1997; Amador et al., 2006), and in flows over transverse rib-roughness (Okamoto et al., 1993; Cui et al., 2003). At higher elevations, the water-phase turbulence intensities were noticeably larger next to the inception point than further downstream, highlighting the turbulent nature of the RVF region. For the chamfered steps, slightly larger Tu_p values were identified at the upstream edge than at the downstream edge. Overall, no significant cavity and step edge effects were observed on the distributions of water-phase turbulence.

4.3. Total pressure time scales

The longest connections of total pressure fluctuations in the flow may be characterised by the total pressure autocorrelation time scale:

$$T_{xx,p} = \int_0^{\tau_{R_{xx,p=0}}} R_{xx,p}(\tau)\, d\tau \quad (15)$$

where $R_{xx,p}$ is the normalised autocorrelation coefficient of the total pressure signal and τ is the time lag. $T_{xx,p}$ is a measure of the average longitudinal size of the energy-containing eddies subject to effects of coherent density fluctuations.

Fig. 11 shows typical distributions of dimensionless total pressure time scales at step edges for the various configurations. All configurations, except for model *IIa*, exhibited the largest total pressure time scales close to the pseudo-bottom, reaching a dimensionless value of approximately 0.2. The more scattered $T_{xx,p}$ data in model *IIa* appeared to be associated with increased flow instabilities caused by the cavity blockage. Significant time scales were sometimes observed next to the inception point, highlighting the large-scale instabilities in that region. For model *III*, subtly

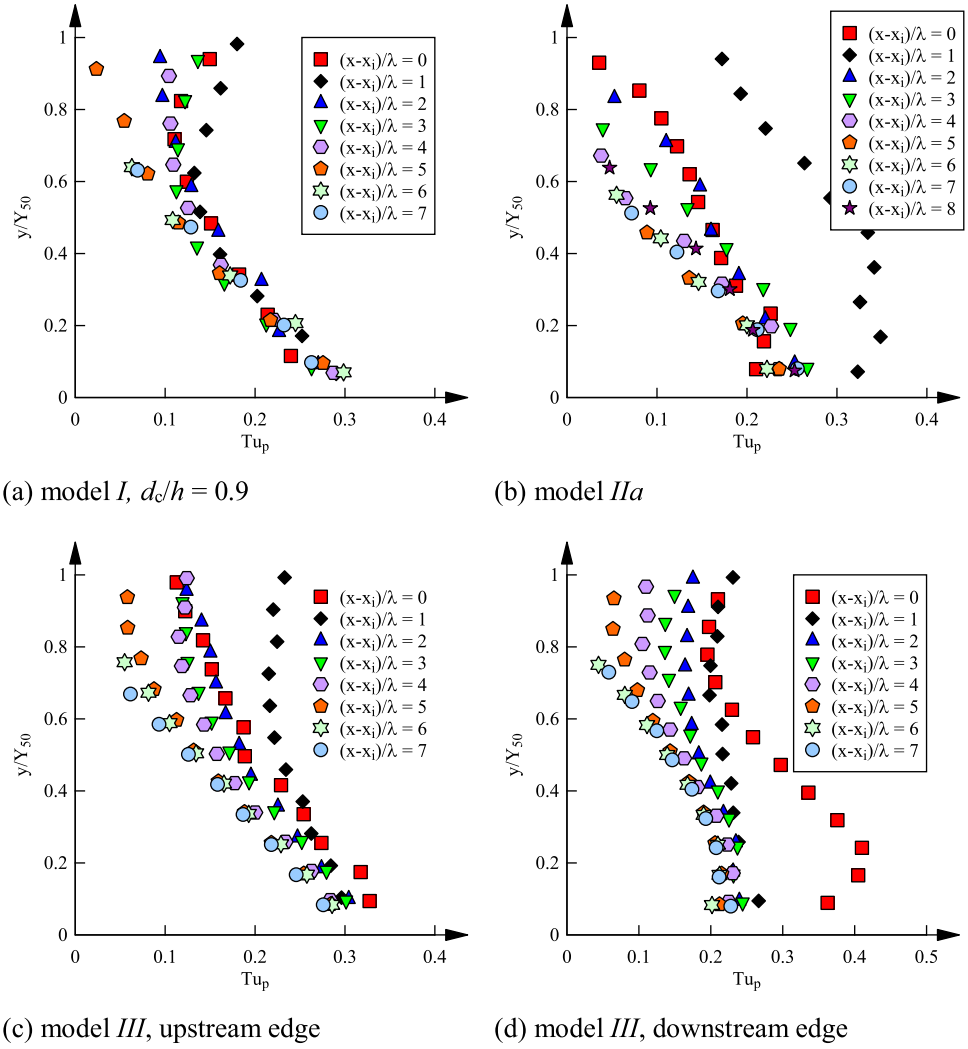

Fig. 10. Water-phase turbulence intensity distributions at step edges in chutes with various step roughness types. Flow conditions: model *I*/*II*: $d_c/h = 0.9$, $Re = 3.4 \times 10^5$; model *IIb*: $d_c/h = 0.94$, $Re = 3.6 \times 10^5$; $\theta = 45°$.

larger $T_{xx,p}$ values were identified at the upstream edge than at the downstream edge. The observation could be linked to a reduction in turbulent production along the chamfer edge because of smaller velocity gradients. At sufficient distance downstream of the inception point (i.e. $(x\text{-}x_i)/\lambda > 2$), the data in both models *I* and *III* exhibited some self-similarity. Hence the energy-containing structures might have reached a state of pseudo-dynamic equilibrium, despite that uniform equilibrium flow conditions were not achieved. Importantly, the findings demonstrated some large impact of cavity blockage on the spatial homogeneity of the flow.

The dimensionless $T_{xx,p}$ profile displayed a marked change at about $y/Y_{50} = 0.8 - 1$. This implied a physical demarcation in flow properties about this region, potentially underpinned by structural changes in the two-phase turbulence patterns. In the lower region (i.e. $y/Y_{50} < 0.8 - 1$), the $T_{xx,p}$ values were dominantly of the order 0.1, which was comparable to a roughness timescale T_k defined as:

$$T_k = \frac{k}{U_{sl}} \quad \text{for } 0 \leq y/Y_{50} < 0.8{-}1 \tag{16}$$

where k is the roughness height projection normal to the pseudo-bottom, and U_{sl} is the convection velocity in the shear layer. Since $T_{xx,\,p} \sim k_T/\varepsilon$ (k_T: turbulent kinetic energy; ε: dissipation) (Pope 2000), the observation highlighted the importance of the lower aerated flow region for turbulent production, and the absence of roughness characteristics for $y/Y_{50} > 0.8 - 1$.

Fig. 12 examines the relationship between the dimensionless total pressure time scale $T_{xx,p}$ and integral air-water time scale $T_{xx,c}$ in stepped chutes *I* and *IIa*. The data revealed a strong correlation between the two variables for $y/Y_{50} \geq 1$ ($R = 0.79$), and almost no correlation for $y/Y_{50} < 1$ ($R = 0.13$), where R is the normalised correlation coefficient. If the total pressure signal is simply expressed as a sum of air and water components:

$$f(t) = f_a(t) + f_w(t) \tag{17}$$

and assuming that the air and water components are independent, it follows that:

$$R_{xx,p}(\tau) = R_{xx,a}(\tau) + R_{xx,w}(\tau) \tag{18}$$

$$T_{xx,p} = T_{xx,c} + T_{xx,w} \tag{19}$$

where $R_{xx,w}$ and $T_{xx,w}$ are the water-phase contributions to the autocorrelation function and integral time scale of the total pressure signal. For $y/Y_{50} \geq 1$, the high correlation between $T_{xx,p}$ and $T_{xx,c}$ implies that $T_{xx,w} \approx 0$. Hence the water-phase contribution to the total pressure signal in this region was approximately a white noise with a flat power spectrum (i.e. the autocorrelation function of the water phase signal is a delta function). The finding confirmed a lack of water-phase structure in the upper flow region. Note that the data might be skewed in very low void fraction regions due to unreliability of the phase-detection probe.

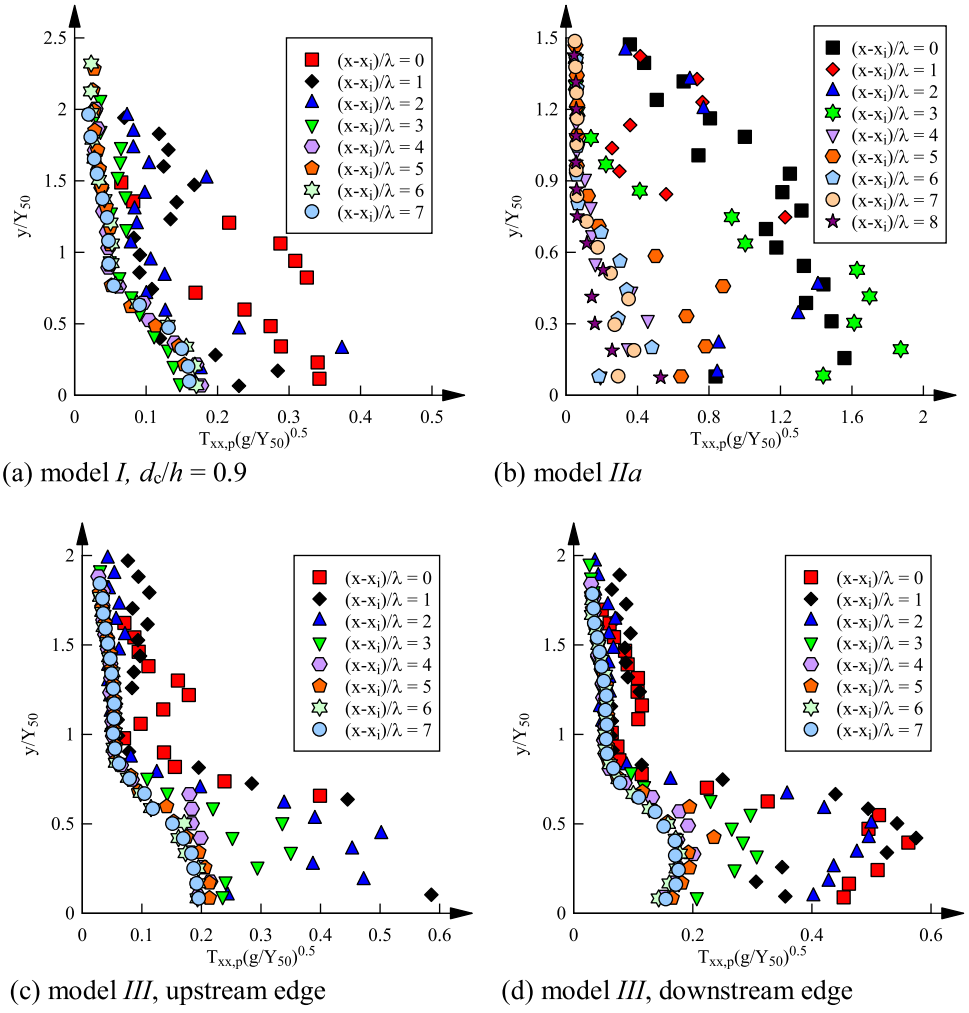

Fig. 11. Total pressure time scale distributions at step edges in chutes with various step roughness types. Flow conditions: model *I*/*II*: $d_c/h = 0.9$, $Re = 3.4 \times 10^5$; model *IIb*: $d_c/h = 0.94$, $Re = 3.6 \times 10^5$; $\theta = 45°$.

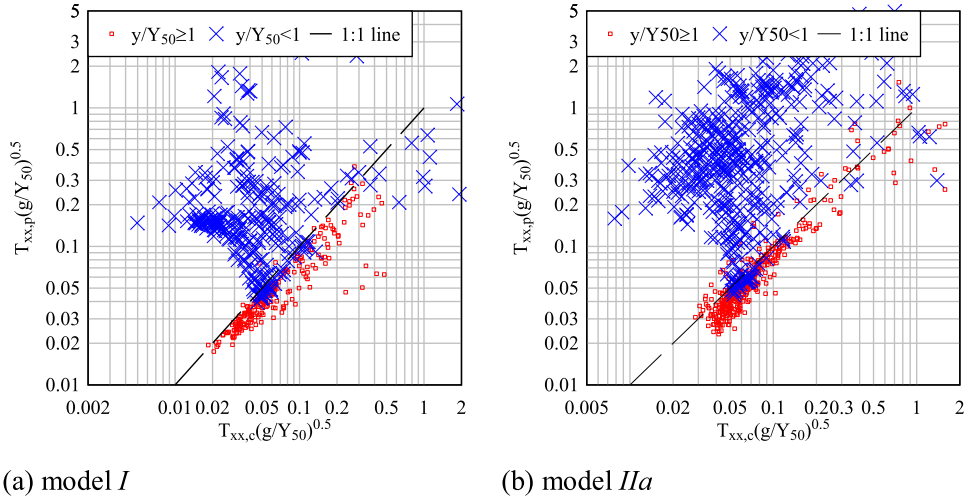

Fig. 12. Relationship between $T_{xx,p}$ and $T_{xx,c}$ at step edges in models *I* and *IIa*. Flow conditions: Model *I*: $d_c/h = 0.9$ – 1.7, $Re = 3.4$ – 8.8×10^5; Model *IIa*: $d_c/h = 0.94$ – 1.75, $Re = 3.6$ – 9.1×10^5; $\theta = 45°$.

5. Conclusion

Skimming air-water flow properties were carefully examined in a stepped chute configured with triangular steps, chamfered steps, and partially blocked step cavities. Interactions between the air and water phases were investigated with a dual-tip phase-detection probe mounted side-by-side with a total pressure transducer. The effects on skimming flow air-water properties induced by step and cavity geometry modifications were characterised.

Void fraction distributions in all models showed a reasonable agreement with analytical solutions of the advection-diffusion equation. The no-flux boundary condition imposed on the chamfer surface stipulated an air boundary layer growth, which could lead to a reduction in skin friction. All bubble count rate data followed a characteristic shape with a maximum occurring next to $C \approx 0.5$. The interfacial velocity data followed a two-tier distribution with a demarcation at $y/Y_{50} \approx 1$. In comparison to the unmodified step geometry, steeper and flatter step edge velocity profiles were respectively observed for the chamfered steps and partially blocked cavities. Correlation analyses identified significant interfacial fluctuations and large air-water structures at $y/Y_{50} \approx 1$ as well as next to the pseudo-bottom, which might be sensitive to step and cavity geometry modifications. The data indicated that uniform equilibrium conditions were not achieved in the present studies.

Simultaneously acquired void fraction and total pressure signals permitted individual examinations of the component phases. Significant total pressure fluctuations were identified throughout the flow column, resulting from water-phase turbulent fluctuations coupled with rapid phase changes. The water-phase turbulence levels were comparable to those reported for the clear water flow region, and were substantially less than the interfacial turbulence levels. The total pressure time scale distributions implied a physical demarcation about $y/Y_{50} = 0.8 - 1$, where the upper region was characterised by a lack of coherent water-phase structures. The partial cavity blockage also appeared to result in increased instabilities in the aerated flow region.

The present investigation indicated some implications for stepped chute design due to step edge and cavity modifications. The chamfers led to some reduction in air entrainment, slightly raised interfacial turbulence levels, and a steeper mean velocity profile next to the pseudo-bottom. The partial cavity blockages were observed to cause flow instabilities and an increased presence of large-scale structures in the overflow, likely resulting from modifications to the vortex shedding dynamics. Importantly, the results highlighted the turbulent nature and extremely complex air-water interactions in aerated skimming flows over stepped roughness.

Acknowledgements

The authors thank Jason Van Der Gevel and Steward Matthews (University of Queensland, Australia) for their technical assistance. The financial support of Australian Research Council (Grant DP120100481) is acknowledged. The first author was a recipient of Australian Postgraduate Award.

Appendix A. List of symbols

C	time-averaged void fraction (-)
C_{mean}	depth-averaged void fraction (-)
D_a	average diffusivity (m^2/s)
D_t	turbulent diffusivity (m^2/s)
D_0	dimensionless diffusivity (-)
d_c	critical depth (m)
F	bubble count rate (Hz)
g	gravity constant (m/s^2)
h	vertical step height (m)
K	integration constant (-)
k	step roughness height (m)
k_T	turbulent kinetic energy (m^2/s^2)
l	horizontal step length (m)
N_{50}	power law exponent (-)
P_t	time-averaged total pressure (Pa)
p_t'	fluctuating total pressure (Pa)
Q	water discharge (m^3/s)
q_w	unit discharge of water (m^2/s)
R	normalised correlation coefficient (-)
$R_{xx,a}$	air-phase contribution to $R_{xx,p}$ (-)
$R_{xx,c}$	normalised autocorrelation coefficient of a void fraction signal (-)
$R_{xx,p}$	normalised autocorrelation coefficient of a total pressure signal (-)
$R_{xx,w}$	water-phase contribution to $R_{xx,p}$ (-)
Re	Reynolds number (-)
T_{aw}	average interfacial travel time between two probe tips (s)
T_k	roughness time scale (s)
$T_{xx,a}$	air-phase contribution to $T_{xx,p}$ (s)
$T_{xx,c}$	streamwise autocorrelation timescale based on a void fraction signal (s)
$T_{xx,p}$	streamwise autocorrelation timescale based on a total pressure signal (s)
$T_{xx,w}$	water-phase contribution to $T_{xx,p}$ (s)
$T_{0.5}$	time lag for which normalised autocorrelation of the leading tip equals 0.5 (s)
Tu_{aw}	interfacial turbulence intensity (-)
Tu_p	water-phase turbulence intensity estimated from synchronised total pressure and void fraction signals (-)
t	time (s)
U_{aw}	time-averaged interfacial velocity (m/s)
U_{sl}	convection velocity in shear layer (m/s)
U_w	time-averaged water velocity (m/s)
U_{50}	time-averaged interfacial velocity corresponding to $C = 0.5$ (m/s)
u_{aw}'	fluctuating interfacial velocity (m/s)
x	streamwise coordinate (m)
Y_{50}	elevation normal to the pseudo-bottom where $C = 0.5$ (m)
Y_{90}	elevation normal to the pseudo-bottom where $C = 0.9$ (m)
y	normal coordinate (m)

Greek symbols

Δx	streamwise separation between probe tips (m)
ε	disspation rate (m^2/s^3)
θ	chute slope (°)
λ	streamwise separation between adjacent steps (m)
τ	time lag between two signals (s)
$\tau_{0.5}$	time lag for which the normalised cross-correlation between two probe tips equals 0.5 (s)

Functions

erfc	complementary error function

Acronyms

CDF	cumulative distribution function
DPP	dual-tip phase-detection probe
FS	full scale
GVF	gradually varied flow
PDF	probability density function
RVF	rapidly varied flow
TPT	total pressure transducer

References

Amador, A., Sánchez-Juny, M., Dolz, J., 2006. Characterization of the nonaerated flow region in a stepped spillway by PIV. *J. Fluids Eng.*, ASME 128 (6), 1266–1273. doi:10.1115/1.2354529.

Carosi, G., Chanson, H., 2006. Air-water time and length scales in skimming flow on a stepped spillway. Application to the spray characterisation. Division of Civil Engineering, The University of Queensland, Brisbane, Australia *Report No. CH59/06*, July, 142.

Chanson, H., 1993. Stepped spillway flows and air entrainment. *Can. J. Civil Eng.* 20 (June(3)), 422–435. doi:10.1139/l93-057.
Chanson, H., 1997. Air bubble entrainment in open channels. Flow structure and bubble size distributions. *Int. J. Multiphase Flow* 23 (1), 193–203. doi:10.1016/S0301-9322(96)00063-8.
Chanson, H., 2001b. Hydraulic design of stepped spillways and downstream energy dissipators. *Dam Eng.* 11 (4), 205–242.
Chanson, H., 2002. Air-water flow measurements with intrusive phase-detection probes. Can we improve their interpretation? *J. Hydraul. Eng.*, ASCE 128 (3), 252–255. doi:10.1061/(ASCE)0733-9429(2002)128:3(252).
Chanson, H., 2004. Drag reduction in skimming flow on stepped spillways by aeration. *J. Hydraul. Res.* IAHR 42 (3), 316–322.
Chanson, H., Carosi, G., 2007. Advanced post-processing and correlation analyses in high-velocity air-water flows. *Environ. Fluid Mech.* 7 (6), 495–508.
Chanson, H., Toombes, L., 2002. Air-water flows down stepped chutes: turbulence and flow structure observations. *Int. J. Multiphase Flow* 28 (11), 1737–1761. doi:10.1016/s0301-9322(02)00089-7.
Crowe, C., Sommerfeld, M., Tsuji, Y, 1998. Multiphase Flows with Droplets and Particles. CRC Press, Boca Raton, USA, p. 471. (ISBN 0-8493-9469-4).
Cui, J., Patel, V.C., Lin, C., 2003. Large-eddy simulation of turbulent flow in a channel with rib roughness. *Int. J. Heat Fluid Flow* 24 (3), 372–388. doi:10.1016/s0142-727x(03)00002-x.
Felder, S., Chanson, H., 2009. Turbulence, dynamic similarity and scale effects in high-velocity free-surface flows above a stepped chute. *Exp. Fluids* 47 (1), 1–18. doi:10.1007/s00348-009-0628-3.
Felder, S., 2013. Air-water flow properties on stepped spillways for embankment dams. Aeration, energy dissipation and turbulence on uniform, non-uniform and pooled stepped chutes *Ph.D. Thesis*. School of Civil Engineering, The University of Queensland, Brisbane, Australia.
Felder, S., Chanson, H., 2014a. Triple decomposition technique in air–water flows: application to instationary flows on a stepped spillway. *Int. J. Multiphase Flow* 58, 139–153. doi:10.1016/j.ijmultiphaseflow.2013.09.006, & 3 videos.
Felder, S., Chanson, H., 2014b. Effects of step pool porosity upon flow aeration and energy dissipation on pooled stepped spillways. *J. Hydraul. Eng.* ASCE 140 (4), 11. doi:10.1061/(ASCE)HY.1943-7900.0000858, Paper 04014002.
Felder, S., Chanson, H., 2016. Air–water flow characteristics in high-velocity free-surface flows with 50% void fraction. *Int. J. Multiphase Flow* 85, 186–195. doi:10.1016/j.ijmultiphaseflow.2016.06.004.
Gonzalez, C.A., Chanson, H., 2008. Turbulence manipulation in embankment stepped chute flows: an experimental study. *Eur. J. Mech. B/Fluids* 27 (4), 388–408. doi:10.1016/j.euromechflu.2007.09.003.
Ohtsu, I., Yasuda, Y., 1997. "Characteristics of flow conditions on stepped channels. In: Proc. 27th IAHR Congress. Theme D, San Francisco, USA, pp. 583–588.
Okamoto, S., Seo, S., Nakaso, K., Kawai, I., 1993. Turbulent shear flow and heat transfer over the repeated two-dimensional square ribs on ground plane. *J. Fluids Eng.* ASME 115 (4), 631–637. doi:10.1115/1.2910191.
Pope, S., 2000. Turbulent Flows. Cambridge University Press, Cambridge, U.K..
Rao, N.S.L., Kobus, H.E., 1971. Characteristics of self-aerated free-surface flows. Water and Waste Water Current Research and Practice, Vol.10. Eric Schmidt Verlag, Berlin.
Stephenson, D., 1988. Stepped energy dissipators. In: Proc. Intl Symp. on Hydraulics for High Dams. IAHR, Beijing, China, pp. 1228–1235.
Toombes, L., Chanson, H., 2008. Interfacial aeration and bubble count rate distributions in a supercritical flow past a backward-facing step. *Int. J. Multiphase Flow* 34 (5), 427–436.
Wood, I.R., 1985. Air water flows. In: Proc. 21st IAHR Congress. Melbourne, Australia, pp. 18–29.
Wood, I.R., 1991. Air entrainment in free-surface flows. IAHR Hydraulic Structures Design Manual No. 4. Balkema Publ, Rotterdam.
Wuthrich, D., Chanson, H., 2015. Aeration performances of a gabion stepped weir with and without capping. Environ. Fluid Mech. 15 (4), 711–730.
Zhang, G., Chanson, H., 2016a. Gabion stepped spillway: interactions between free-surface, cavity, and seepage flows. *J. Hydraul. Eng.* ASCE 142 (5), 5. doi:10.1061/(ASCE)HY.1943-7900.0001120, Paper 06016002.
Zhang, G., Chanson, H., 2016b. Interactions between free-surface aeration and total pressure on a stepped chute. *Exp. Therm. Fluid Sci.* 74, 368–381. doi:10.1016/j.expthermflusci.2015.12.011.
Zhang, G., Chanson, H., 2017. Self-aeration in smooth and stepped chutes. *Environ. Fluid Mech.* 17 (1), 27–46. doi:10.1007/s10652-015-9442-z.